



# Flow Strength Measurements of Additively Manufactured and Wrought 304L Stainless Steel up to 200 GPa Stresses

P. E. Specht<sup>1</sup> · J. L. Brown<sup>1</sup> · D. P. Adams<sup>1</sup>

Received: 31 January 2024 / Accepted: 7 August 2024  
© Society for Experimental Mechanics, Inc 2024

## Abstract

Magnetically-driven, shockless-compression experiments were performed to peak stresses approaching 200 GPa on both a direct energy deposition, additively manufactured (AM) and conventionally, wrought-processed 304L stainless steel to compare their thermodynamic and constitutive responses. Velocimetry measurements were used to infer the response of the 304L stainless steel samples during shockless-compression and release from peak stress. A self-consistent, inverse Lagrangian analysis technique was used to determine the isentrope of each sample to peak compression, while a wave profile analysis method was used to estimate the flow strength, shear modulus, and bulk modulus from the unloading from peak stress. The thermodynamic response of both stainless steels were similar and consistent with current equation of state (EOS) formulations up to 200 GPa. The flow strength, shear modulus, and bulk modulus measurements were also similar between stainless steel variants. The flow strength measurements in the AM material showed evidence of more sample-to-sample variability, particularly at pressures above 100 GPa. This was hypothesized to result from the large grain size imparted during printing. The flow strength and shear modulus measurements of both stainless steels deviated from current calibrations of the Steinberg-Guinan-Cochran and Preston-Tonks-Wallace constitutive models. The bulk modulus values extracted for both stainless steels deviated from those predicted by a Vinet EOS fit to the extracted isentropes, particularly at pressures above 100 GPa. This was found to result from the assumption of linearity of the bulk modulus with pressure in the Vinet model. The observed response of the 304L stainless steel shows a quadratic dependence of the bulk modulus with pressure, which is hypothesized to result from the formation of martensite during loading.

**Keywords** Shockless compression · Additive manufacturing · Stainless steel · Isentrope · Flow strength

## Introduction

Stainless steel is commonly used in engineering applications due to its high strength and corrosion resistance. The most common stainless steels are austenitic, having a face-centered cubic (FCC) structure. Austenitic stainless steels, like type 304 and 316, are also common alloys for additive manufacturing (AM) [1–3]. However, the rapid cooling rates produced by the AM process generate microstructures more akin to a welded material than a conventional wrought material [4]. AM microstructures tend to have a periodic grain structure, and in cubic systems, like 304 stainless steel, a fiber texture with the  $\langle 100 \rangle$  orientation aligned with

the direction of heat flow (i.e. the build direction) [5, 6]. Understanding how the AM fabrication process alters the material microstructure and influences the observed material response, termed process-structure–property (PSP) relationships, is essential for wider adoption of AM materials in engineering applications. This is especially true for 304 stainless steel which exhibits a complex microstructural response to mechanical loading, having large elastic anisotropy between orientations [7] and undergoing a strain-induced phase transformation [8–13], twinning [9, 11, 12, 14–16], load shedding [17, 18], and dynamic recrystallization [14, 19, 20].

Numerous past studies have investigated the role microstructure plays in the mechanical response of stainless steels at quasi-static [1, 6, 17, 21–24], intermediate [12, 13, 25–31], and high strain-rates [15, 16, 32–38]. At high strain-rates, most prior work focused on the elastic–plastic and failure response at stresses below 10 GPa. In these studies, the AM stainless

✉ P. E. Specht  
pespech@sandia.gov

<sup>1</sup> Sandia National Laboratories Albuquerque, Albuquerque, NM 87185-1189, USA

steel exhibited a higher Hugoniot elastic limit (HEL) [32, 33] than wrought material, with evidence of anisotropy due to the underlying microstructure [32, 33, 38]. Lamb et al. [38] and Wise et al. [32] saw anisotropy in the HEL and failure response of laser powered bed fusion (LPBF) 316L and Laser engineered net shaping (LENS<sup>®</sup>) 304L stainless steel, respectively.

In order to facilitate the development of more representative model calibrations, there is a need for more information on the response of austenitic stainless steel at higher stresses where the mechanical response is dominated by different mechanisms. Studies at intermediate strain-rates [31], suggest that a saturation point is quickly reached in the strain-hardening of austenitic stainless steel. At higher stresses where the strain is larger, pressure-hardening is expected to take over as the dominant hardening mechanism. Additionally, at stresses above 100 GPa, the amount of equation of state (EOS) data on 304L stainless steel is limited [34, 39] and no flow strength data exists. Experiments at higher stresses are necessary to determine if the underlying microstructure influences the thermodynamic and constitutive response in 304L stainless steel at stresses above 100 GPa.

In the presented work, a series of shockless-compression experiments to a peak stress approaching 200 GPa were used to measure the EOS and flow strength of both AM and wrought 304L stainless steel. To quantify the degree of anisotropy in the AM 304L stainless steel, two orthogonal directions in the AM billet were studied: one parallel and one perpendicular to the build direction. These two orientations provide bounding cases for understanding the influence of the grain structure on the response of AM 304L stainless steel, since they have very disparate microstructures. The response of each orientation of the AM 304L stainless steel and that of the wrought material were then compared to each other and existing model calibrations in the literature to identify any variations. Section “[Experimental Method](#)” describes the experimental method including the initial material microstructure (Sect. “[Materials Under Study](#)”), shockless-compression experimental design (Sect. “[Magnetic Shockless-Compression Experiments](#)”), and the self-consistent Lagrangian analysis technique (Sect. “[Self-Consistent Inverse Lagrangian Analysis](#)”). Section “[Experimental Results and Discussion](#)” presents the experimental results and discussion for the measured isentropes (Sect. “[Isentrope Measurements](#)”) and the flow strength, shear modulus, and bulk modulus measurements (Sect. “[Flow Strength, Shear Modulus, and Bulk Modulus Measurements](#)”).

## Experimental Method

### Materials Under Study

#### Ingot-derived Wrought 304L Stainless Steel

The wrought 304L stainless steel was ingot-derived, remelted material with a controlled sulfur, weld-critical composition (Honeywell Federal Manufacturing and Technology, Kansas City, Missouri). The composition of the wrought material as determined using a combination of inductively-coupled plasma mass-spectroscopy (ICP-MS), gas fusion and combustion, and optical emission spectroscopy is provided in Table 2. The wrought material was primarily austenite with 1.2% ferrite (body-centered cubic, BCC) as determined with Ferretiscope<sup>®</sup> and X-ray diffraction measurements. An inverse pole figure (IPF) map of the wrought microstructure obtained with electron backscatter diffraction (EBSD), is shown in Fig. 1. The wrought microstructure was composed of equiaxed, austenite grains roughly 50  $\mu\text{m}$  in size with elongated ferrite stringers aligned with the extrusion axis of the billet. No evidence of measurable porosity was found.

The measured bulk properties of the wrought material are provided in Table 1. The density was obtained using an Archimedes method. The longitudinal,  $c_l$ , and transverse,  $c_s$ , wave speeds were measured at 10 and 5 MHz, respectively. The shear moduli,  $G$ , bulk moduli,  $K$ , and Poisson’s ratios,  $\nu$ , listed in Table 1 were calculated from the measured density and wave speeds.

Samples were extracted from the center of the wrought billet via electrical discharge machining (EDM) to provide similar mechanical characteristics, as a variation in hardness with billet radius was identified in the as-received material [1]. All experimental samples were ground and polished to final thickness to remove the brass contamination in the heat-affected zone from the EDM wire. All wrought samples were loaded parallel to the billet extrusion axis.

**Table 1** Measured bulk properties of the wrought and LENS<sup>®</sup> 304L stainless steel. All errors represent one standard deviation

	Wrought	X-Cut AM	Z-Cut AM
Density ( $\text{g}/\text{cm}^3$ )	7.882 (0.015)	7.881 (0.015)	7.881 (0.015)
$c_l$ ( $\text{km}/\text{s}$ )	5.742 (0.049)	5.784 (0.066)	5.993 (0.085)
$c_s$ ( $\text{km}/\text{s}$ )	3.132 (0.025)	3.356 (0.213)	3.374 (0.120)
$G$ (GPa)	77.33 (1.25)	89.14 (11.28)	89.81 (6.41)
$K$ (GPa)	156.83 (4.74)	144.86 (16.23)	163.35 (11.75)
$\nu$	0.288 (0.007)	0.241 (0.052)	0.266 (0.026)

**Table 2** Elemental composition (wt. %) of the wrought and LENS<sup>®</sup> 304L stainless steel as determined via ICP-MS, gas fusion and combustion, and optical emission spectroscopy along with that of the

starting powder feedstock (as supplied by Carpenter Powder Products). The remainder is Fe

	C	Cr	Cu	Mn	Mo	N	Ni	O	P	S	Si	V
Wrought	0.013	19.5	–	1.5	0.027	0.049	10.1	–	0.015	0.015	0.58	0.02
LENS <sup>®</sup>	0.010	18.8	0.03	1.49	0.04	0.075	10.28	0.023	0.007	0.007	0.51	0.02
Feedstock	0.015	19.07	0.03	1.55	0.04	0.089	10.38	0.017	0.006	0.006	0.5	0.02

### LENS<sup>®</sup> 304L Stainless Steel

The AM 304L stainless steel billets were printed on wrought 304L stainless steel base plates using a custom, LENS<sup>®</sup>, direct energy deposition system located at Pennsylvania State University [40]. The feedstock was nitrogen-atomized, micro-melt powder obtained from Carpenter Powder Products with particle sizes ranging from 10 to 44  $\mu\text{m}$ . The powder was injected at a flow rate of 23 g/min into the incident continuous-wave IPG Photonics<sup>®</sup> YLR-12000-L ytterbium fiber laser operating at a power of 3.8 kW and a beam diameter of 4 mm. A parallel hatch scan pattern was used, as illustrated at the bottom of Fig. 1, with a hatch spacing of 1.925 mm, a scan speed of 63.5 cm/min and a build rate of 1.27 mm/layer. An inert argon atmosphere was used with less than 110 ppm of oxygen.

The composition of the as-received powder, as given by the supplier, and the as-printed material, measured using ICP-MS, gas fusion and combustion, and optical emission spectroscopy, are provided in Table 2. The as-printed LENS<sup>®</sup> material had slightly less chromium and slightly more oxygen than the feedstock, which was attributed to vaporization and oxidation during the printing process, respectively. When compared to the wrought material, the LENS<sup>®</sup> material had significantly more nitrogen content due to the powder being atomized in a nitrogen atmosphere. This was of particular interest given the tendency for stainless steel to exhibit nitrogen solution hardening [41].

Since the LENS<sup>®</sup> material was fabricated in a layer-by-layer fashion, it was expected to have a periodic microstructure. As a result, two orthogonal directions of the LENS<sup>®</sup> billets were investigated. We define a coordinate system relative to the build laser for the LENS<sup>®</sup> billets that is consistent with the ASTM standard [42]. The positive Z direction defines the build direction and is parallel with, but opposite to, the build laser. The positive X direction defines the dominant scan line direction, while the positive Y direction is the hatch direction. This is summarized with the schematic at the bottom of Fig. 1. Figure 1 shows IPF maps for microstructures in both the Z (Z-Cut) and X (X-Cut) orientations.

In the IPF maps of the LENS<sup>®</sup> 304L stainless steel, the periodic nature of the microstructure is evident. The difference in grain-size and texture when compared to the wrought

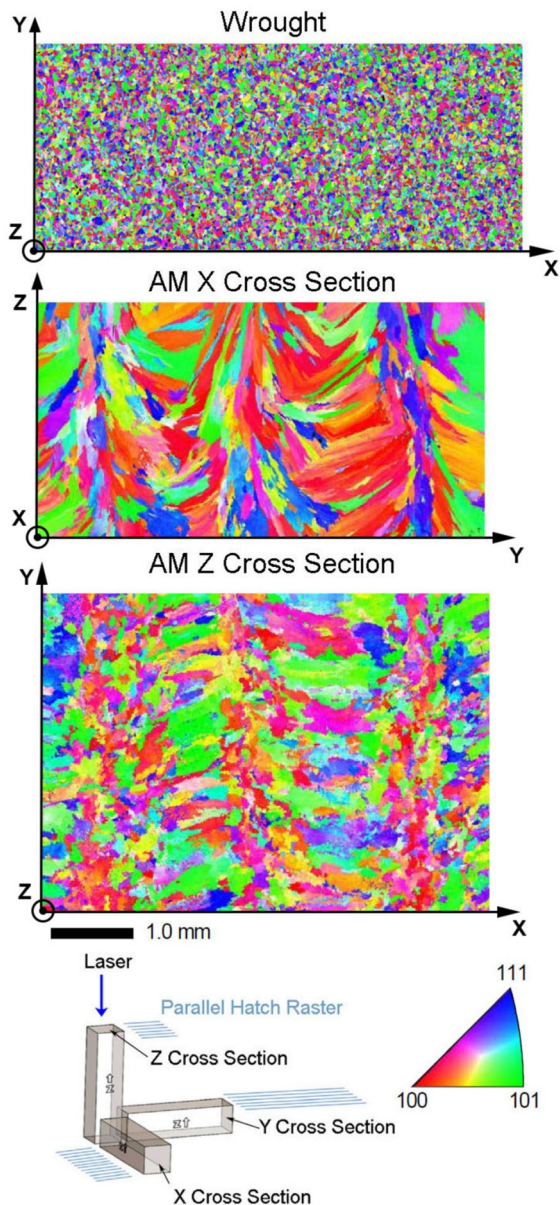


**Fig. 1** IPF maps of the wrought, Z-Cut, and X-Cut material. The IPF maps are all colored relative to the positive horizontal direction: positive X for the wrought and Z-Cut, and positive Y for the X-Cut. The bottom image shows a schematic of the parallel hatch build pattern used for the LENS<sup>®</sup> 304L stainless steel

material is also evident. The LENS<sup>®</sup> material exhibited large, elongated grains (approximately 1 mm) that oriented epitaxially from one layer to the next. These grains showed evidence of a preferred crystalline  $\langle 100 \rangle$  texture in the build direction commonly seen in AM cubic metals [5]. Neutron diffraction measurements [17] on the LENS<sup>®</sup> material found 2.3% [17] ferrite, roughly twice the amount in the wrought material. Higher resolution EBSD images of the LENS<sup>®</sup> material indicated mosaicity in the grains. This sub-grain structure requires more geometrically necessary dislocations, which was confirmed with higher dislocation densities found via neutron diffraction [17].

The measured bulk properties of the LENS<sup>®</sup> material are provided in Table 1. The density, measured using an Archimedes method, indicates essentially zero porosity. As a result, no effects of porosity were considered in this work. The wave speeds of the LENS<sup>®</sup> material, measured in the same manner as the wrought material, and the resulting elastic properties calculated from them, have more error. This was attributed to the large grain size and texturing in the LENS<sup>®</sup> material, since it is more likely that a few, randomly oriented grains dominate the measured response. Austenitic stainless steels exhibit large anisotropy in elastic properties for individual crystals [7].

## Magnetic Shockless-Compression Experiments

Shockless, or ramp, compression provides a continuous measurement near the isentrope of a material up to peak stress [43]. The resulting curve is often termed a quasi-isentrope, since some irreversible phenomena like plastic work heating are present [43]. Measurements along the isentrope are useful for constraining tabular EOS models, since they provide data at high pressures but relatively low temperatures. Additionally, the elastic–plastic transition during release from peak stress provides an estimate of the flow strength, shear modulus and bulk modulus of the material assuming purely isotropic hardening [44, 45]. Such measurements are valuable for validating and/or calibrating constitutive models at high strain-rates.

A total of 8 magnetic shockless-compression experiments were conducted on the Z pulsed power accelerator [46, 47] at Sandia National Laboratories and followed the method outlined in prior studies [43, 45, 48–50]. A schematic of the Z accelerator target is given in Fig. 2a. The experiments utilized a stripline geometry [51], which consisted of two parallel panels connected at the top to produce a low-inductance, short-circuit load. A time-varying current,  $\mathbf{J}$ , was pushed through the target generating a strong magnetic field,  $\mathbf{B}$ , in the anode-cathode (AK) gap between the panels. The cross product of this magnetic field with the time-varying current pulse produced a stress wave,  $\sigma$ , normal to the electrode, as illustrated in Fig. 2b. This stress wave propagated into

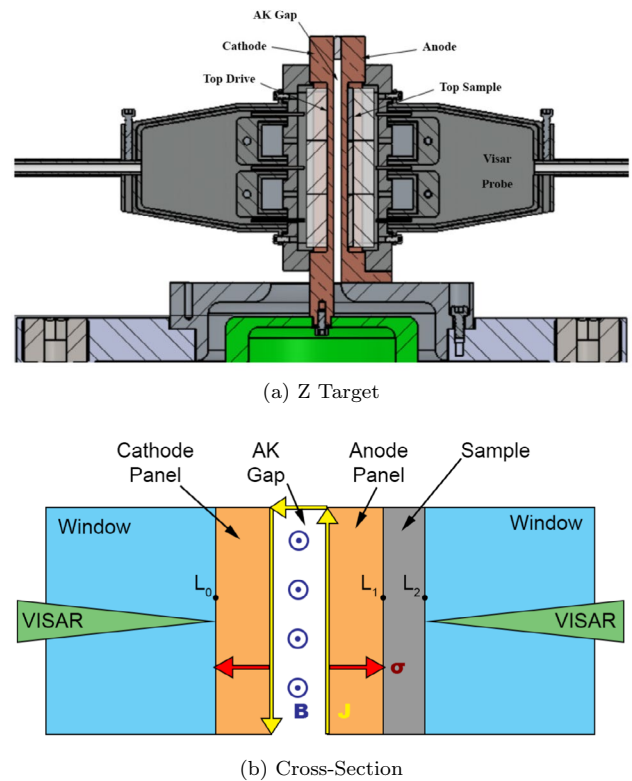


**Fig. 2** A schematic of the magnetic shockless-compression experiments performed on the Z pulsed power accelerator (a). The stripline geometry contains three samples on the anode panel and three drive measurements on the cathode panel. A cross-sectional view (b) shows the interactions of the current ( $\mathbf{J}$ ), magnetic field ( $\mathbf{B}$ ), and stress wave ( $\sigma$ ) during the experiment. Positions  $L_0$ ,  $L_1$ , and  $L_2$  were used in the TF-SCLA method for determining the isentrope

the sample ahead of the magnetic diffusion front, enabling the compression of the sample to high stresses prior to vaporization.

Copper panels with a nominally 2 mm floor thickness were used for both the anode and cathode and were separated by a 2 mm AK gap. The panel shapes were tapered to reduce variations in the magnetic field experienced along the height of the panel [50]. For most experiments (i.e. Z3090, Z3129, Z3187, Z3257, Z3324, Z3340, and Z3420), the anode panel contained three 15 mm x 15 mm square, nominally 1.5 mm thick 304L stainless steel samples: one wrought, one X-Cut LENS<sup>®</sup>, and one Z-Cut LENS<sup>®</sup>. One experiment, Z3113, contained only one Z-Cut LENS<sup>®</sup> sample. The specific locations of each sample were varied between experiments to eliminate the possibility of systematic errors in the measured properties due to location on the anode panel. Each sample was backed by a 15 mm x 15 mm square, nominally 6 mm thick  $\langle 100 \rangle$ -oriented LiF window. The cathode panel was used for back calculating the magnetic field opposite each sample [51, 52], which is discussed in more detail in Sect. “[Isentrope Measurements](#)”, and contained only a

15 mm x 15 mm square, nominally 6 mm thick (100)-oriented LiF window. All LiF windows had a 250 nm vapor-deposited Al coating on the interface side and an anti-reflective coating for 523 nm light on the free surface to improve the quality of the VISAR (velocity interferometry system for any reflector) [53] measurements. All VISAR measurement employed three velocity-per-fringe (VPF) constants.

The time-varying current pulses were designed following the criteria outlined by Brown et al. [45]. The rise times were chosen to generate a smooth ramp wave and ensure the only wave interactions that need accounting for are due to reflections off the window altering the incoming stress wave. The sample dimensions were also chosen to ensure that edge waves did not influence the observed release response, as verified by two-dimensional (2D) magnetohydrodynamic (MHD) simulations in ALEGRA [54].

### Self-Consistent Inverse Lagrangian Analysis

Detailed descriptions of the analysis of shockless-compression experiments are located elsewhere [44, 45, 55–57]. Only a brief description of the analysis procedure is presented here.

The response of a material compressed by a single, steady pressure wave that is uniaxial in strain, is described through direct Lagrangian analysis (DLA) [58]. Measuring the time-dependent *in situ* material velocity,  $u^*$ , at two locations, enables the determination of the longitudinal Lagrangian wave speed,  $c_L$ , as a function of the *in situ* material velocity. Integrating the conservation of mass and momentum equations in Lagrangian coordinates provides the longitudinal stress,  $\sigma_x$ , and density,  $\rho$ .

$$\frac{d\rho}{\rho^2} = \frac{du^*}{\rho_0 c_L(u^*)} = d\epsilon \quad (1)$$

$$d\sigma_x = \rho_0 c_L(u^*) du^* \quad (2)$$

Here,  $\rho_0$ , refers to the initial material density, and  $\epsilon$  is the engineering strain.

In practice, the *in situ* material velocity is not measured, usually due to a lack of transparency of the sample. Most experiments make velocity measurements at the free surface of the sample or at an interface between the sample and a transparent window. Inverse Lagrangian analysis (ILA) provides a method for converting interface velocities,  $u$ , to *in situ* material velocities [44, 45].

For this work, a transfer function-based, self-consistent Lagrangian analysis (TF-SCLA) [44, 45] technique was used to determine the *in situ* material velocity from the measured interface velocity. A series of one-dimensional (1D) forward simulations were performed using an assumed compressive behavior (i.e.  $\sigma_x(\rho)$ ) for the material to estimate  $u$  and  $u^*$  and

define the transfer function. The first simulation mimicked the experimental cathode panel and had a Lagrangian tracer at the panel/window interface (i.e. position  $L_0$  in Fig. 2b). The second simulation mimicked the experimental anode panel and had a Lagrangian tracer located at the sample/window interface (i.e. position  $L_2$  in Fig. 2b). The third simulation assumed a semi-finite sample and had Lagrangian tracers located at the panel/sample interface and at the same coordinates as the sample/window interface (i.e. position  $L_1$  and  $L_2$  in Fig. 2b, respectively). The simulated window and *in situ* velocity profiles at position  $L_2$  were used to define the transfer function at that location. Similarly, the simulated cathode window velocity at position  $L_0$  and the *in situ* velocity at position  $L_1$  were used to define the transfer function at that location, since the anode and cathode had similar thicknesses. While this approach differs from prior work [45], it captured the elastic response in a more representative way.

The impedance difference between the window and sample produce wave reflections from the front of the stress wave that interact with the later time, higher stress portions as it approaches the interface. These interactions are not present in the semi-infinite simulation used to obtain the *in situ* velocity. This leads to a difference in the casual domain of the window and *in situ* velocities that need to be accounted for prior to generating the transfer function [44]. Thus, the time scales of the window and *in situ* velocities are normalized by identifying the times of key features in each trace and then generating a linear relationship between them.

This process generated a numerical mapping between the simulated window and *in situ* velocities. Applying this mapping to the measured interface velocities at the cathode and anode produced “experimental” *in situ* velocities at positions  $L_1$  and  $L_2$  for defining the compressive behavior up to peak stress using DLA. This process was repeated with the updated compressive behavior until convergence.

Upon release from peak stress, the material undergoes an elastic–plastic transition that provides an estimate of flow strength, shear modulus, and bulk modulus of the sample [44, 56, 57]. Since the sample remains under uniaxial strain over the course of the experiment, J2 plasticity theory [59] is assumed to hold and the longitudinal stress,  $\sigma_x(\epsilon)$ , is written as a function of the pressure,  $P(\epsilon)$  and shear stress,  $\tau(\epsilon)$  [60].

$$\sigma_x(\epsilon) = P(\epsilon) + \frac{4}{3}\tau(\epsilon) \quad (3)$$

Assuming a von Mises or Tresca yield criteria, the shear stress is related to the yield strength,  $Y = 2\tau$ . A differential form of the longitudinal stress equation is then written using  $c_L$ , and the Lagrangian bulk wave speed,  $c_B$  [44].

$$d\tau(\epsilon) = \frac{3}{4}\rho_0[c_L^2(\epsilon) - c_B^2(\epsilon)]d\epsilon \quad (4)$$

Changing variables to the material velocity and integrating provides a measure of the change in shear stress upon unloading[61].

$$2\tau = \frac{3}{4}\rho_0 \int_{u_{trans}^*}^{u_{peak}^*} [c_L^2(u^*) - c_B^2(u^*)] \frac{du^*}{c_L(u^*)} \quad (5)$$

Here,  $u_{trans}^*$  is the particle velocity at which bulk plastic unloading begins and  $u_{peak}^*$  is the peak particle velocity achieved at a position  $L_2$ . In the experiment, there is some degree of attenuation, which is accounted for with the following assumption [55, 62]

$$2\tau_{atten} \approx \frac{3}{4}\rho_0 [c_L^2(u_{peak}^*) - c_B^2(u_{trans}^*)] \frac{\Delta u_{peak}^*}{c_{L,peak}} \quad (6)$$

where  $\Delta u_{peak}^*$  is the difference in peak material velocities at positions  $L_1$  and  $L_2$ , and  $c_{L,peak}$  is longitudinal Lagrangian wave speed at  $u_{peak}^*$ . Following the convention of Brown et al. [44], the recorded flow strengths are all reported at the mean pressure of the quasi-elastic unloading region.

Additionally, assuming that the peak wave speeds are representative of the material at peak stress, estimates of the shear and bulk moduli are defined with the following.

$$G = \frac{3}{4}\rho_0(1 - \epsilon_{peak})(c_{L,peak}^2 - c_{B,peak}^2) \quad (7)$$

$$K = \rho_0(1 - \epsilon_{peak})c_{B,peak}^2 \quad (8)$$

Here,  $c_{B,peak}$  is the value given by a quadratic fit to  $c_B$  during bulk plastic loading at  $u_{peak}^*$  to eliminate errors due to relaxation near peak stress [57].

The flow strength extracted from the release is dependent on the location of  $u_{trans}^*$ . This is often not straight forward, given experimental uncertainties and the possibility of kinematic hardening shifting the symmetry axis away from the hydrostat [63]. To provide a more systematic method for defining  $u_{trans}^*$ , an additional simulation was run with a semi-infinite, hydrodynamic sample and a Lagrangian tracer at position  $L_2$ . Comparing the hydrodynamic simulation to the semi-infinite simulation in the TF-SCLA method, which included a constitutive model, provided an estimate for  $u_{trans}^*$  as illustrated in Fig. 3. This novel approach also enabled the automation of the strength analysis, which was necessary for the error estimation method employed.

### TF-SCLA Error Analysis

To estimate the error in the isentropes, flow strengths, and shear and bulk moduli, a Monte Carlo approach was taken similar to prior methods [44, 64], since it is straight forward to implement and inherently conservative. In this

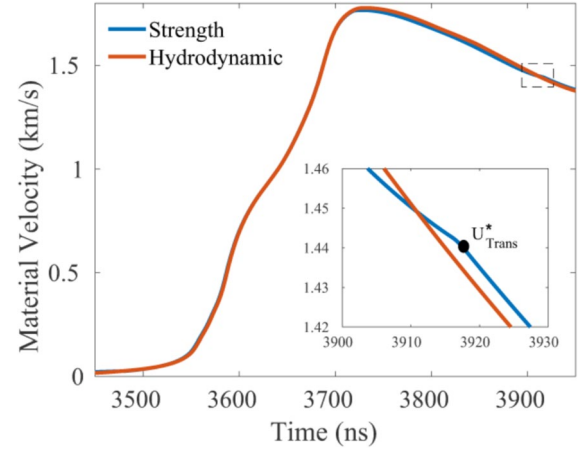


**Fig. 3** Example plot of the material velocities obtained in the 1D MHD simulations for a semi-infinite sample at position  $L_2$  with (strength) and without (hydrodynamic) a constitutive model. The dashed box nominally represents the location of the inset which shows the deviation in response upon release due to the constitutive model and identifies  $u_{trans}^*$

approach, a set of 10,000 1D forward simulations were run to obtain velocity traces for the TF-SCLA analysis treating all uncertainties as random and uncorrelated. Each set of simulations had differing panel, sample, and glue bond thicknesses as defined by normal distributions to their measured means and standard deviations. Additionally, each set of simulations had a unique scaling factor for the applied magnetic field obtained from a normal distribution with a mean of 1 and a standard deviation of 0.0075. This scaling factor is consistent with prior estimates [44, 64] and approximates the uncertainty in the applied magnetic field resulting from uncertainties in the Cu and LiF models during the unfold process, which is discussed in Sect. “Experimental Results and Discussion”.

When performing the TF-SCLA analysis, uncertainties in the initial density and the measured sample/window velocity profile were accounted for. A normal distribution for the initial density was generated from values in Table 1 to define a unique starting point for the integration of the conservation equations for each simulation set. To account for the temporal and velocity uncertainties in the sample/window velocity profile in a straightforward way, a unique scaling factor and time shift were applied to the measured sample/window interface velocity for each simulation set. Both the scaling factor and time shift were described by normal distributions. The scaling factor was determined from the uncertainty in the VISAR measurement (i.e.  $\approx 5\%$  of the VPF) and had a mean of 1 and a standard deviation of 0.005. The time shift applied to the velocity profiles corresponds to the timing accuracy of Z and had a mean of 0 and a standard deviation of 1 ns, which is consistent with prior estimates [44, 64].

This process generated 10,000 isentropes for estimating the uncertainty. While each simulation set does provide  $c_L(u^*)$  upon release for estimating the flow strength and shear and bulk moduli, not every parameter combination yields realistic behavior. As a result, only the simulations with realistic elastic–plastic transitions were used for estimating the uncertainty in the flow strength, shear modulus, and bulk modulus.

## Experimental Results and Discussion

### Measured Interface Velocities

The interface velocities for each 304L stainless steel sample, shifted arbitrarily in time for clarity, are shown in Fig. 4. The interface velocities presented in Fig. 4 were corrected for the change in index of refraction of the LiF window upon compression, using the method developed by Davis et al. [65]. All the velocity profiles exhibited a smooth ramp to peak stress and a distinct change in slope during the release, which represented the elastic–plastic transition.

### Isentrope Measurements

As mentioned previously, the magnetic field incident on the cathode and anode panels remains the same as long as the geometric asymmetries present (i.e. deformation) remain small. For all experiments in the present work, 2D ALEGRA simulations were used to verify the magnetic field experienced by the cathode and anode were identical over the time frame of interest. Thus, the magnetic field determined using the unfold process on the cathode was applied directly to forward simulations of the anode. Additionally, by using the time-varying magnetic field determined from the cathode measurement opposite each sample, any slight differences in the magnetic drive along the length of the panel were accounted for in the analysis [44, 50].

Figure 5 shows the measured interface velocities on the cathode panel, denoted by location as top, middle, and bottom, for the four unique machine settings used in this work. The velocity traces presented in Fig. 5 are shifted in time arbitrarily for clarity and were corrected for the LiF window. All the cathode panel measurements showed good uniformity in loading along the panel, with the peak velocity of the top location being approximately 2% higher than the bottom location. However, given the pairwise nature of the TF-SCLA method, this deviation is not a relevant error. The uncertainty over each sample is the error of interest and is much lower. With the exception of Z3187, identical machine configurations were used for additional measurements: Z3090, Z3113, and Z3129, Z3257 and Z3324, and

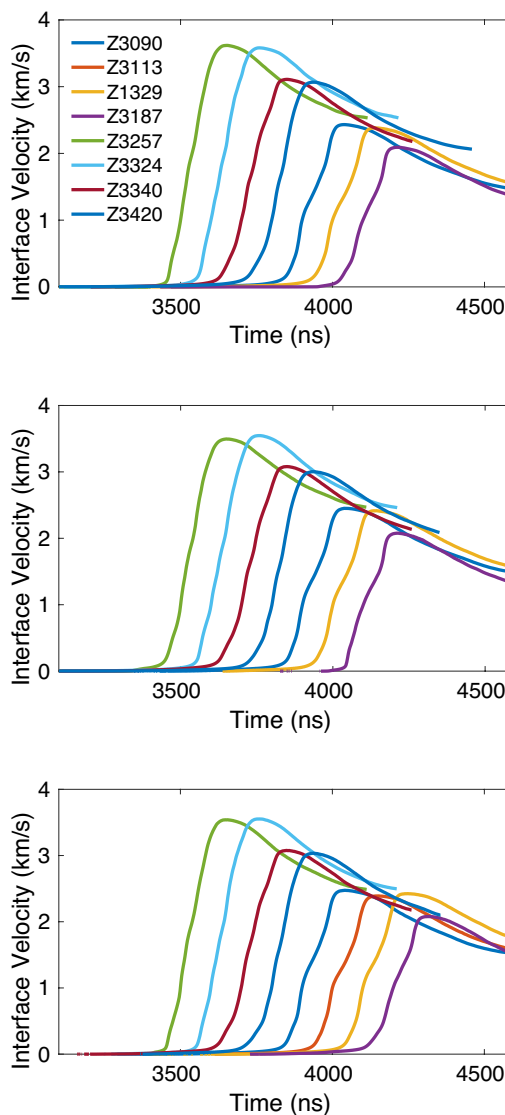


**Fig. 4** Corrected interface velocities for each type of 304L stainless steel sample: wrought (top), X-Cut LENS<sup>®</sup> (middle), and Z-Cut LENS<sup>®</sup> (bottom). All the velocity traces are arbitrarily shifted in time for clarity

Z3340 and Z3420. Figure 6 shows a comparison of the mean drive measurements for Z3090 and Z3129, illustrating minimal machine jitter ( $\approx 2\%$ ). Given the roughly 1% uncertainty in the interface velocity at peak, this enabled complementary measurements at near identical conditions for assessing sample-to-sample variability.

To calculate the magnetic field from the cathode drive measurements, the unfold procedure outline by Lemke et al. [51, 52] was used. The unfold procedure assumes that the Cu panel and LiF window are material standards with well-defined EOS and constitutive responses. Using that assumption, the magnetic field experienced at each height along the cathode for each experiment was

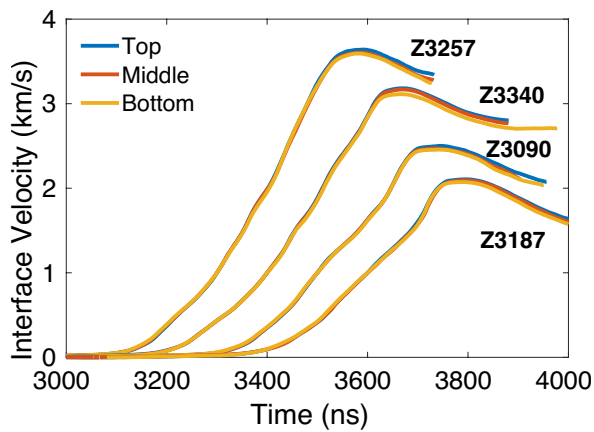


**Fig. 5** Corrected interface velocities along the cathode panel for the four unique machine configurations employed. Good uniformity in the magnetic loading was observed in all experiments. Each set of velocity traces are arbitrarily shifted in time for clarity

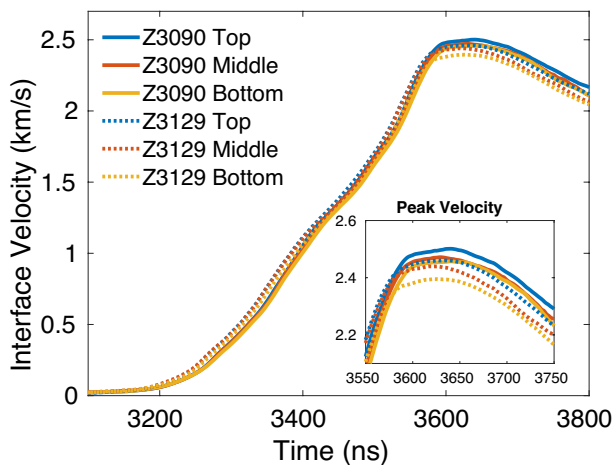


**Fig. 6** Corrected mean interface velocities along the cathode panel in experiments Z3090 and Z3129. The measured mean velocities were within 2% of each other with identical machine configurations as shown by the inset of the peak velocity

determined though optimization of 1D MHD simulations in LASLO [66].

An initial guess of the magnetic field was fit with 143 spline points and used as the boundary condition for the 1D LASLO simulation. DAKOTA [67] was used to alter the magnetic field until the simulated interface velocity matched the measured interface velocity to within a desired tolerance. In these simulations, the Cu panel was modeled with the 3325 SESAME tabular EOS [68], the Steinberg-Guinan-Cochran (SG) strength model [69, 70], an internally-calibrated elastic-plastic model [71], and a tabular electrical conductivity [72]. The LiF window was modeled with the SESAME 7271v3 tabular EOS [65, 73], and a calibrated SG model [74] employing a modified shear modulus to

approximate the elastic-plastic response [44]. A constant electrical and thermal conductivity was used for the LiF since the magnetic field does not diffuse into it during the experiment.

The magnetic field calculated on the cathode opposite each sample was then used in the forward simulations for the TF-SCLA, as described in Sect. “Self-Consistent Inverse Lagrangian Analysis”, to determine the isentrope of the sample. A Vinet fit to the isentrope defined by the SESAME 4270 EOS table [75] was taken as an initial guess for the 304L stainless steel EOS, and a rate-independent SG strength model [70] was used to approximate the constitutive response. A constant thermal and electrical conductivity was used for the 304L stainless steel, since the magnetic field does not diffuse into the sample during the experiment.

For samples with significant glue bonds (i.e. above 5  $\mu$  m), the glue layer was explicitly accounted for in the forward simulations. The glue was assumed to be hydrodynamic and modeled with the SESAME 7602 EOS table [76]. A constant thermal and electrical conductivity was used for the glue.

Integration of the Lagrangian conservation equations provided the stress as a function of density, which is typically termed a quasi-isentrope. However, having the isentrope, or the relationship between pressure and density, is more useful for EOS calibrations. The pressure can be inferred from the stress if a von Mises or Tresca yield criteria is assumed and the yield strength at each stress is known. For this work, the SG calibration for 304 stainless steel [70] was used to approximate the yield strength at each stress for calculating the pressure. In addition to subtracting  $\frac{2}{3}$  of the yield strength, the thermal contribution to the pressure [77], assuming a Taylor-Quinney coefficient of 1, was also subtracted from the stress to obtain the pressure. This process aims to account for the main sources of entropy to produce the isentropes reported in this work.

The isentropes inferred for each sample are given in Fig. 7 and compared to the SESAME 4270 EOS table [75]. The SESAME 4270 EOS table matches the response of the wrought and LENS<sup>®</sup> 304L stainless steel well at the pressures investigated. The similar response between the wrought and LENS<sup>®</sup> 304L stainless steel support the common notion that the bulk, thermodynamic response is not influenced by the texture and/or grain size of the material. The underlying microstructure is expected to influence the deviatoric component of the stress. The estimated error bounds for the mean isentrope for each configuration in pressure-density space, calculated from all samples using a T-distribution and the standard error, are represented by the gray bands in Fig. 7.

The error estimate of the mean isentrope has abrupt jogs, which correspond to transitions from pressure regions with more experiments to those with less. The isentropes for each sample were fit with a Vinet EOS [78–80], assuming



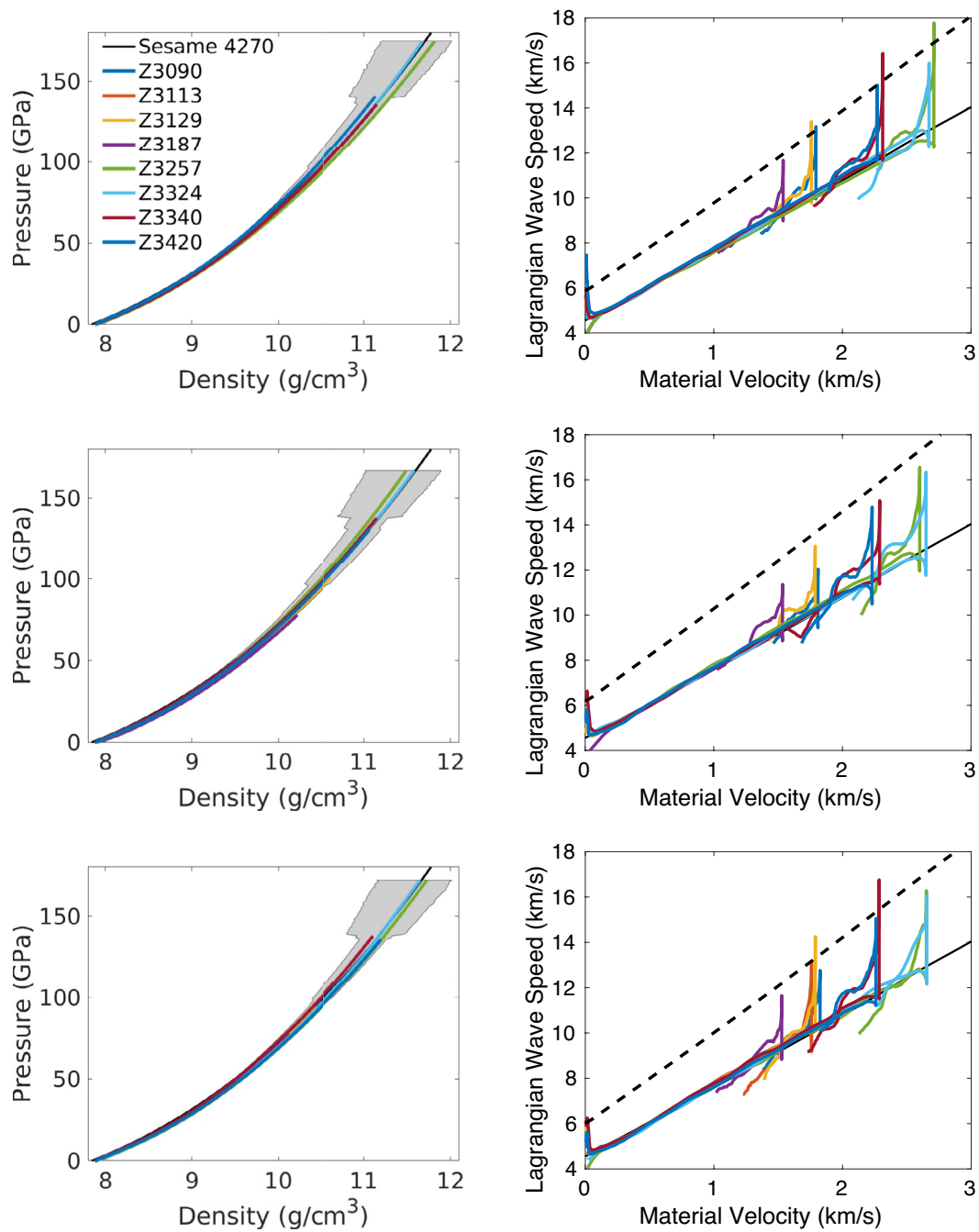


**Fig. 7** Comparison of the isentropes in  $P$ - $\rho$  (left side) and  $c_L$ - $u^*$  (right side) space for the wrought (top), X-Cut LENS<sup>®</sup> (middle), and Z-Cut LENS<sup>®</sup> (Bottom), which are all well approximated by the SESAME 4270 EOS table. The gray bands in the  $P$ - $\rho$  plots represent the 95%

confidence bounds based on the standard error for the isentropes. The dashed line in the  $c_L$ - $u^*$  plots represents the estimated elastic wave speed using the  $c_l$  and  $v$  provided in Table 1

a coefficient of thermal expansion of  $17 \mu\text{m/m/K}$ . For the Vinet fits, both the initial isothermal bulk modulus,  $B_0$ , and its pressure derivative,  $(\partial B/\partial P)_0$ , were treated as fitting parameters. The parameters for the Vinet fits, along with their uncertainty, for the Wrought, X-Cut LENS<sup>®</sup>, and Z-Cut LENS<sup>®</sup> material are given in Table 3 along with a fit for all samples. The fits for the wrought and LENS<sup>®</sup> material were

essentially the same, with the X-Cut LENS<sup>®</sup> material exhibiting only slightly more uncertainty. Additionally, the initial bulk moduli obtained were consistent with those reported in Table 1, despite treating it as a fitting parameter.

The larger uncertainty in the Vinet fit for the X-Cut LENS<sup>®</sup> material is not surprising given the microstructure shown in Fig. 1. In the X-Cut orientation, the grains

**Table 3** Vinet parameters obtained fitting all isentropes extracted from the Monte Carlo error method. All uncertainties represent one standard deviation

Material	$B_0$ (GPa)	$(\partial B/\partial P)_0$
Wrought	156.97 (6.63)	5.72 (0.37)
X-Cut LENS <sup>®</sup>	153.56 (9.92)	5.84 (0.42)
Z-Cut LENS <sup>®</sup>	154.68 (4.86)	5.79 (0.35)
All Samples	155.05 (7.47)	5.79 (0.38)

were elongated and approximately 1 mm in length, near the 1.5 mm thickness of the sample. Thus, it is possible to have only a few grains dominating the response leading to small deviations between samples.

The right side of Fig. 7 shows the Lagrangian wave speed versus *in situ* material velocity for all the 304L stainless steel variants along with that extracted from the SESAME 4270 EOS table for bulk loading. Once again, there was good agreement between the measured response and that predicted by the SESAME 4270 EOS table upon loading.

### Flow Strength, Shear Modulus, and Bulk Modulus Measurements

Most of the Lagrangian wave speeds on the right side of Fig. 7 exhibited an initial elastic response followed by bulk plastic loading. A few experiments exhibited a lower initial elastic wave speed, which was attributed to complications from thicker glue bonds. The dashed lines in Lagrangian wave speed versus *in situ* material velocity space, shown on the right side of Fig. 7, represent the estimated elastic wave speed assuming the initial value and Poisson's ratio given in Table 1. Overall, there was decent agreement between this estimate of the elastic wave speed with those found upon release in each experiment. Most experiments exhibited a clear elastic–plastic transition upon unloading which was used to estimate the flow strength, shear modulus and bulk modulus of each sample, as described in Sect. “Self-Consistent Inverse Lagrangian Analysis”.

The resulting flow strengths and shear moduli reliably extracted from the samples are presented in Fig. 8 and listed in Table 4. Since many of the distributions for the flow strengths and shear moduli were not normal, the error bars in Fig. 8 and the values given in Table 4 represent the 5<sup>th</sup> and 95<sup>th</sup> percentiles. The flow strengths extracted for the wrought and LENS<sup>®</sup> material were similar, with no clear signs of anisotropy in the LENS<sup>®</sup> material. This suggests the grain structure of 304L stainless steel is not a significant factor in the flow stress at pressures above 100 GPa. However, the LENS<sup>®</sup> material may exhibit more sample-to-sample variability. It is possible that the grain size, structure, and texture have some influence on the response, especially

given the close proximity of the grain size to the sample thickness. Figure 1 shows an area large enough to extract 9 samples (i.e. a 3 x 3 grid). It is not hard to envision two LENS<sup>®</sup> samples with vastly different microstructures. The same cannot be said of the wrought material. Although, this hypothesis is based on the mean values reported in Table 4. It is clear from Fig. 8, that the uncertainties of each measurement in the LENS<sup>®</sup> material overlap. Combining this with the low number of data points (i.e. 2-3), it is impossible to draw firm conclusions.

Figure 8 also shows the predicted values using the rate-independent SG [70] and the Preston-Tonks-Wallace (PTW) [81] calibrations. The SG model prediction in Fig. 8 used the SESAME 4270 EOS table to approximate the pressure, temperature and density response along the isentrope. The PTW model prediction in Fig. 8 was found using a 1D LASLO simulation. The simulations used the SESAME 4270 EOS table and a pressure boundary condition that produced a constant  $2e5 \text{ s}^{-1}$  strain-rate, which was the average strain-rate through all experiments. To complete the PTW model, the melt temperature and shear modulus as a function of density were assumed to follow the same form as the SG model [69]. The SG model calibration, while in most error bars, appears to slightly underpredict the flow strength and shear modulus, particularly above 100 GPa. The PTW model, while doing a better job than the SG model to represent the flow strength, slightly overpredicts the results, particularly at pressures below 100 GPa. The shear modulus predicted by the PTW model is similar to that of the SG model, which is expected given the use of identical forms for the density dependence.

The underprediction of the SG model at pressures above 100 GPa is consistent with prior measurements in Ta [82]. In Ta, this was attributed to slip-mediated plasticity breaking the assumption of a linear dependence of the shear modulus with pressure. However, the better agreement of the PTW module using the same form for the shear modulus suggests that the under prediction of the SG calibration may be due to something else, like strain-rate dependence. Regardless of the reason, a refined SG model fit was obtained through modifying the pressure-hardening parameter,  $A$  (i.e.  $\frac{1}{G_0} \frac{dG}{dP}$ ), since most flow stresses recorded are above the 2.5 GPa assumed by the model as the limit of strain-hardening. A rate-independent SG model with the pressure-hardening increased by a factor of 1.5, shown by the dashed line in Fig. 8, better represents the data.

Figure 9 shows the bulk moduli obtained from each experiment along with that predicted by the Vinet fit for all samples given in Table 3. Similar to the flow and shear moduli, the error bars in Fig. 9 represent the 5<sup>th</sup> and 95<sup>th</sup> percentiles. The gray band in Fig. 9 represents the 95% confidence bounds of the Vinet fit. The bulk moduli of the wrought and LENS<sup>®</sup>

**Table 4** Flow strengths, shear and bulk moduli inferred from each experiment. Error is presented as the 5th and 95th percentiles

Experiment	Mean Pressure			Flow Strength			Shear Modulus			Bulk Modulus		
	(GPa)			(GPa)			(GPa)			(GPa)		
	Best	5%	95%	Best	5%	95%	Best	5%	95%	Best	5%	95%
Wrought												
Z3090	87.97	85.91	90.23	3.12	2.44	4.37	297.15	188.61	484.30	585.49	572.42	628.09
Z3129	85.41	84.31	88.47	3.12	2.23	3.70	340.36	231.63	438.83	573.00	560.86	625.67
Z3187	70.56	67.30	71.79	2.17	1.68	3.08	217.21	164.01	279.37	529.70	506.80	547.26
Z3257	–	–	–	–	–	–	–	–	–	–	–	–
Z3324	159.13	158.43	163.82	4.75	3.75	5.04	316.28	299.12	482.71	796.86	796.56	894.15
Z3340	127.86	125.34	131.92	4.15	2.45	4.66	527.51	275.78	549.41	756.64	724.11	840.17
Z3420	125.03	122.18	127.20	4.10	3.26	4.91	353.03	279.86	512.02	729.33	724.04	828.17
AM X-Cut												
Z3090	91.57	88.93	92.46	2.22	1.74	3.65	174.31	154.18	325.47	583.59	574.18	616.58
Z3129	89.04	86.83	91.36	2.67	1.97	3.90	292.83	181.52	360.66	608.07	582.98	655.20
Z3187	70.53	68.10	72.10	2.37	1.86	3.40	191.34	115.88	262.81	544.21	503.20	556.14
Z3257	154.13	151.67	160.36	6.50	5.01	7.52	421.02	329.49	700.62	781.18	770.785	916.80
Z3324	158.73	156.21	165.98	3.43	1.46	3.60	400.94	145.70	423.124	945.80	888.25	1021.72
Z3340	126.43	125.19	131.04	3.68	1.60	3.89	356.43	146.16	470.94	786.03	768.79	910.26
Z3420	122.21	118.16	123.04	4.54	3.03	5.68	352.18	220.96	489.02	722.38	662.30	725.24
AM Z-Cut												
Z3090	93.20	90.67	94.62	2.17	1.89	3.51	233.88	171.20	360.24	614.06	585.05	648.66
Z3113	87.50	86.42	89.43	3.20	2.47	3.85	296.00	251.35	398.24	554.26	527.25	567.11
Z3129	89.76	88.31	92.17	3.36	2.69	4.25	425.53	291.56	558.77	568.09	552.85	597.10
Z3187	71.07	69.94	72.44	2.45	1.92	3.17	221.25	182.47	285.56	511.00	487.27	521.44
Z3257	157.21	152.93	160.87	5.04	3.95	6.94	383.99	202.29	704.94	787.99	770.44	872.29
Z3324	158.67	157.21	165.46	5.04	2.79	5.26	338.92	242.05	513.18	836.89	813.965	955.03
Z3340	127.45	126.16	131.26	5.70	3.97	5.92	577.13	381.58	581.31	728.57	697.40	772.19
Z3420	124.45	123.68	128.54	4.13	2.35	4.23	376.21	190.65	525.62	752.93	713.03	823.70

material are all similar but consistently lower than that predicted by the Vinet fit, especially above 100 GPa. This discrepancy is related to the inherent assumption of the Vinet model of a linear dependence of the bulk modulus with pressure. Figure 9 also shows the bulk modulus calculated during loading for the wrought and LENS<sup>®</sup> material in experiment Z3324 (i.e.  $\rho_0 c_B(u)^2$ ), which obtained the highest pressure, as dashed lines. The calculated bulk modulus for experiment Z3324 suggests a quadratic relationship between the bulk modulus and the pressure, which matches the extracted bulk moduli well. This was why a quadratic fit was used to define  $c_{B,peak}$  in Sect. “Self-Consistent Inverse Lagrangian Analysis”. This quadratic dependence is hypothesized to result from the formation of strain-induced martensite during deformation.

## Conclusions

A series of magnetically-driven, shockless-compression experiments were performed on Sandia National Laboratories’ Z machine to peak stresses approaching 200 GPa on both wrought and LENS<sup>®</sup> 304L stainless steel to measure their thermodynamic and constitutive response. Two orthogonal directions in the LENS<sup>®</sup> 304L stainless steel were studied to look for anisotropy in the response: one parallel to the build direction (Z-Cut) and one perpendicular to the build direction (X-Cut). The isentropes obtained using a TF-SCLA analysis method for both the wrought and LENS<sup>®</sup> 304L stainless steel were in good agreement

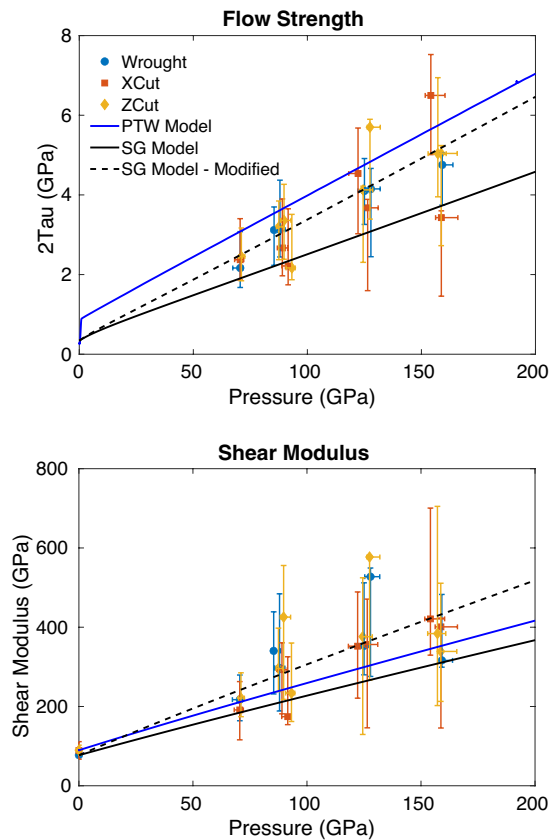


**Fig. 8** Flow strength (top) and shear modulus (bottom) measurements obtained from the unloading behavior. Error bars represent the 5<sup>th</sup> and 95<sup>th</sup> percentiles. The solid blue and black lines are the current PTW and SG constitutive model calibrations for 304 stainless steel, respectively [70, 81]. The dashed line is a modified SG model with the pressure-hardening parameter,  $A$ , increased by a factor of 1.5

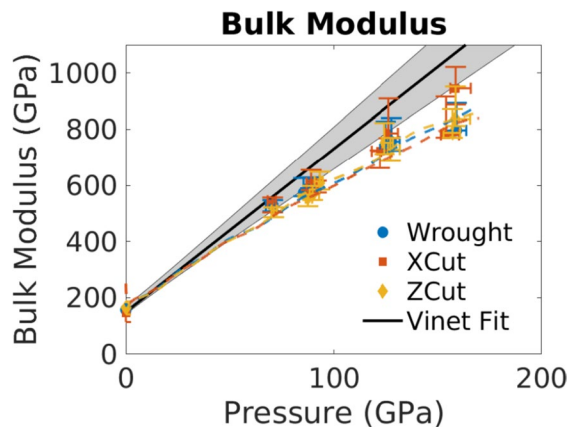


**Fig. 9** Bulk moduli obtained from the unloading behavior compared to the Vinet fit obtained from the isentropes. Error bars represent the 5<sup>th</sup> and 95<sup>th</sup> percentiles. The gray band represents the 95% confidence interval of the Vinet fit. The dashed lines are the bulk modulus calculated during loading for experiment Z3324, which achieved the highest pressure. The extracted bulk moduli are slightly under the Vinet fit at pressures above 100 GPa but match the bulk modulus calculated in experiment Z3324

with each other and the isentrope predicted by the SES-AME 4270 EOS table. The isentropes for all 304L stainless steel samples were reasonably well approximated by a Vinet EOS with a bulk modulus of  $155.05 \pm 7.47$  GPa and a pressure derivative of  $5.79 \pm 0.38$ .

The flow strengths, shear moduli, and bulk moduli of the wrought and LENS<sup>®</sup> material were estimated using the release behavior from peak stress. The flow strengths, shear moduli, and bulk moduli of the wrought and LENS<sup>®</sup> material were similar at all pressures. No signs of anisotropy in the LENS<sup>®</sup> response was observed despite its highly textured, periodic grain structure. The only potential influence of the underlying LENS<sup>®</sup> microstructure on the observed response was higher sample-to-sample variability in the LENS<sup>®</sup> material. This was hypothesized to result from the large grain size in the LENS<sup>®</sup> material, which approached the sample thickness. However, more experiments are needed to verify this hypothesis.

The flow strengths and shear moduli were compared to values predicted by calibrations to the SG and PTW constitutive models. While both predictions were within the error bars of most flow strength and shear modulus values, both failed to represent the response well over the entire pressure regime. The SG model underpredicted the flow strength above 100 GPa, while the PTW model overpredicted the flow strength below 100 GPa. Increasing the pressure-hardening parameter by a factor of 1.5 in the SG model provided values more aligned with the experimental data over the entire pressure regime.

The bulk moduli obtained from the release behavior in the wrought and LENS<sup>®</sup> material were consistently below the values predicted by the Vinet EOS fit to the isentropes, particularly at pressures above 100 GPa. This discrepancy was attributed to the Vinet model's assumption of a linear dependence of the bulk modulus with pressure. A quadratic dependence of the bulk modulus with pressure was observed in both the wrought and LENS<sup>®</sup> 304L stainless steel. This discrepancy between the Vinet model and the observed results was hypothesized to result from the formation of strain-induced martensite during loading.

**Acknowledgements** The authors would like to thank Todd Palmer at Pennsylvania State University for printing the LENS<sup>®</sup> material for this study. The authors would also like to thank the entire Z team for the construction and execution of these experiments. Sandia National Laboratories is a multi-mission laboratory managed and operated by National Technology & Engineering Solutions of Sandia, LLC (NTESS), a wholly owned subsidiary of Honeywell International Inc., for the U.S. Department of Energy's National Nuclear Security Administration (DOE/NNSA) under contract DE-NA0003525. This written work is authored by an employee of NTESS. The employee, not NTESS, owns the right, title and interest in and to the written work and is responsible for its contents. Any subjective views or opinions that might be expressed in the written work do not necessarily represent the views of the U.S. Government. The publisher acknowledges that the U.S. Government retains a non-exclusive, paid-up, irrevocable,

world-wide license to publish or reproduce the published form of this written work or allow others to do so, for U.S. Government purposes. The DOE will provide public access to results of federally sponsored research in accordance with the DOE Public Access Plan.

**Data availability** The data that support the findings of this study are available from the corresponding author upon reasonable request.

## Declarations

**Conflict of interest** The authors have no conflicts to disclose.

## References

- Adams D, Reedlunn B, Maquire M, Song B, Carroll J, Bishop J, Wise J, Kilgo A, Palmer T, Brown D, Clausen B (2019) "Mechanical response of additively manufactured stainless steel 304L across a wide range of loading conditions", Tech. Rep. SAND2019-7001 (Sandia National Laboratories)
- Weaver J, Livescu V, Mara N (2020) A comparison of adiabatic shear bands in wrought and additively manufactured 316L stainless steel using nanoindentation and electron backscatter diffraction. *J Mater Sci* 55:1738
- Murr L, Gaytan S, Ramirez D, Martinez E, Hernandez J, Amato K, Shindo P, Medina P, Wicker R (2012) Metal fabrication by additive manufacturing using laser and electron beam melting technologies. *J Mater Sci Technol* 28:1
- Davis S, Vitek J, Hebble T (1987) Effect of rapid solidification on stainless-steel weld metal microstructures and its implication on the Schaeffler diagram. *Weld J* 66:S289
- Verhoeven J (1991) Fundamentals of physical metallurgy. Wiley, USA
- Charmi A, Falkenberg R, Ávila L, Mohr G, Sommer K, Ulbricht A, Sprengel M, Saliwan Neumann R, Skrotzki B, Evans A (2021) Mechanical anisotropy of additively manufactured stainless steel 316L: an experimental and numerical study. *Mat Sci Eng A* 799:140154
- Kikuchi M (1971) Elastic anisotropy and its temperature dependence of single crystals and polycrystals of 18-12 type stainless steel. *Trans J I M* 12:417
- Hecker S, Stout M, Staudhammer K, Smith J (1982) Effects of strain state and strain rate on deformation induced transformations in 304 stainless steel: part I. magnetic measurements and mechanical behavior. *Metall Trans A* 13A:619
- Kestenbach H-J, Meyers M (1976) The effect of grain size on the shock-loading response of 304-type stainless steel. *Metall Trans A* 7A:1943
- Lee W-S, Lin C-F (2000) The morphologies and characteristics of impact-induced martensite in 304L stainless steel. *Scripta Mater* 43:777
- Murr L, Staudhammer K, Hecker S (1982) Effects of strain state and strain rate on deformation-induced transformation in 304 stainless steel: part II. microstructural study. *Metall Trans A* 13A:627
- Lee W-S, Lin C-F (2002) Comparative study of the impact response and microstructure of 304L stainless steel with and without prestrain. *Metal Mater Trans A* 33A:2801
- Lee W-S, Lin C-F (2001) Impact properties and microstructure evolution of 304L stainless steel. *Mat Sci Eng A* 308:124
- Murr L, Trillo E, Bujanda A, Martinez N (2002) Comparison of residual microstructures associated with impact craters in fcc stainless steel and bcc iron targets: the microtwin versus microband issue. *Acta Mater* 50:121
- Koube K, Kennedy G, Bertsch K, Kacher J, Thoma D, Thadhani N (2022) Spall damage mechanisms in laser powder bed fabricated stainless steel 316L. *Mat Sci Eng A* 851:143622
- Koube K, Sloop T, Lamb K, Kacher J, Babu S, Thadhani N (2023) An assessment of spall failure modes in laser powder bed fusion fabricated stainless steel 316L with low-volume intentional porosity. *J Appl Phys* 133:185903
- Brown D, Adams D, Balogh L, Carpenter J, Clausen B, King G, Reedlunn B, Palmer T, Maguire M, Vogel S (2017) In situ neutron diffraction study of the influence of microstructure on the mechanical response of additively manufactured 304L stainless steel. *Metall Mater Trans A* 48:6055
- Pokharel R, Patra A, Brown D, Clausen B, Vogel S, Gray G III (2019) An analysis of phase stresses in additively manufactured 304L stainless steel using neutron diffraction measurements and crystal plasticity finite element simulations. *Int J Plasticity* 121:201
- Meyers M, Xu Y, Xue Q, Pérez-Prado M, McNelley T (2003) Microstructural evolution in adiabatic shear localization in stainless steel. *Acta Mater* 51:1307
- Xue Q, Heyers M, Nesterenko V (2004) Self organization of shear bands in stainless steel. *Mat Sci Eng A* 384:35
- Wang Z, Palmer T, Beese AM (2016) Effect of processing parameters on microstructure and tensile properties of austenitic stainless steel 304L made by direct energy deposition additive manufacturing. *Acta Mater* 110:226
- Stout M, Follansbee P (1986) Strain rate sensitivity, strain hardening, and yield behavior of 304L stainless steel. *J Eng Mater-T ASME* 108:344
- Chen L, Liu W, Song L (2021) A multiscale investigation of deformation heterogeneity in additively manufactured 316L stainless steel. *Mat Sci Eng A* 820:141493
- Wanni J, Michopoulos J, Achuthan A (2022) Influence of cellular subgrain features on mechanical deformation and properties of directed energy deposited stainless steel 316L. *Addit Manuf* 51:102603
- Nishida E, Song B, Maguire M, Adams D, Carroll J, Wise J, Bishop J, Palmer T (2015) Dynamic compressive response of wrought and additive manufactured 304L stainless steels. *EPJ Web of Conferences* 94:01001
- Song B, Nishida E, Sanborn B, Maquire M, Adams D, Carroll J, Wise J, Reedlunn B, Bishop J, Palmer T (2017) Compressive and tensile stress-strain response of additively manufactured (AM) 304L stainless steel at high strain rates. *J Dynam Behav Mater* 3:412
- Chen J, Wei H, Zhang X, Peng Y, Kong J, Wang K (2021) Flow behavior and microstructure evolution during dynamic deformation of 316L stainless steel fabricated by wire and arc additive manufacturing. *Mater Des* 198:109325
- Chen J, Wei H, Bao K, Zhang X, Cao Y, Peng Y, Kong J, Wang K (2021) Dynamic mechanical properties of 316L stainless steel fabricated by an additive manufacturing process. *Mater Res Technol* 11:170
- Yu H, Chen R, Liu W, Li S, Chen L, Hou S (2022) Dynamic mechanical behavior and microstructural evolution of additively manufactured 316L stainless steel. *J Mater Sci* 57:8425
- Chen H, Li W, Huang Y, Xie Z, Zhu X, Liu B, Wang B (2022) Molten pool effect on mechanical properties in selective laser melting 316 L stainless steel at high-velocity deformation. *Mater Charact* 194:112409
- Chen J, Liu C, Dong K, Guan S, Wang Q, Zhang X, Peng Y, Kong J, Wang K (2023) Crystallographic orientation dependence of dynamic deformation behaviours in additively manufactured stainless steel. *Mater Res Technol* 24:6699
- Wise J, Adams D, Nishida E, Song B, Maguire M, Carroll J, Reedlunn B, Bishop J, Palmer T, Conf AIP (2017) Comparative

- shock response of additively manufactured versus conventionally wrought 304L stainless steel. *Proc* 1793:100015
33. Gray G III, Livescu V, Rigg P, Trujillo C, Cady C, Chen S, Carpenter J, Lienert T, Fensin S (2017) Structure/property (constitutive and spallation response) of additively manufactured 316L stainless steel. *Acta Mater* 138:140
  34. Marsh S (1980) LASL shock hughoniot data LASL shock hughoniot data. University of California Press, California
  35. Whiteman G, Millet J, Bourne N, Conf AIP (2007) Longitudinal and Lateral Stress measurements in stainless steel 304L under 1D shock loading. *Proc* 955:673
  36. Ma L, Liu J, Li C, Zhong Z, Lu L, Luo S (2019) Effects of alloying element segregation bands on impact response of a 304 stainless steel. *Mater Charact* 153:294
  37. Callanan J, Black A, Lawrence S, Jones D, Martinez D, Martinez R, Fensin S (2023) Dynamic properties of 316L stainless steel repaired using electron beam additive manufacturing. *Acta Mater* 246:118636
  38. Lamb K, Koube K, Kacher J, Sloop T, Thadhani N, Babu S (2023) Anisotropic spall failure of additively manufactured 316L stainless steel. *Addit Manuf* 66:103464
  39. van Theil M (1977) (Lawrence Livermore Laboratory) "Compendium of shock wave data", Tech. Rep. UCRL-50108
  40. Tandon R, Wilks T, Gieseke M, Noelke C, Kaierle S, Palmer T (2015), Additive manufacturing of Elektron® 43 alloy using powder bed and direct energy deposition in Proceedings Euro PM 2015 (European Powder Metallurgy Association. Reims, France
  41. Masumura T, Seto Y, Tsuchiyama T, Kimura K (2020) Work-hardening mechanism in high-nitrogen austenitic stainless steel. *Mater Trans* 61:678. <https://doi.org/10.2320/matertrans.H-M2020804>
  42. International A (2013) (ASTM International) "Standard terminology for additive manufacturing - coordinate systems and test methodologies", Tech. Rep. ASTM 52921-13
  43. Davis J-P, Brown J, Knudson M, Lemke R (2014) Analysis of shockless dynamic compression data on solids to multi-megabar pressures: application to tantalum. *J Appl Phys* 116:204903
  44. Brown J, Alexander C, Asay J, Vogler T, Ding J (2013) Extracting strength from high pressure ramp-release experiments. *J Appl Phys* 114:223518
  45. Brown J, Alexander C, Asay J, Vogler T, Dolan D, Belof J (2014) Flow Strength of tantalum under ramp compression to 250 GPa. *J Appl Phys* 115:043530
  46. Savage M, Bennett L, Bliss D, Clark W, Coats R, Elizondo J, LeChien K, Harjes H, Lehr J, Maenchen J, McDaniel D, Pasik M, Pointon T, Owen A, Seidel D, Smith D, Stoltzfus B, Struve K, Stygar W, Warne L, Woodworth J, Mendel C, Prestwich K, Shoup R, Johnson D, Corley J, Hodege K, Wagoner T, Wakefield P (2007). An overview of pulse compression and power flow in the upgraded Z pulsed power driver, in 16th international IEEE pulsed power conference Vol. 1-4 (Albuquerque, NM, 2007) p. 979
  47. Savage M, LeChien K, Lopez M, Stoltzfus B, Stygar W, Artery D, Lott J, Corcoran P (2011) Status of the Z pulsed power driver, in *IEEE Pulsed Power Conference* p. 983
  48. Hall C, Asay J, Knudson M, Stygar W, Spielman R, Pointon T, Reisman D, Toor A, Cauble R (2001) Experimental configuration for isentropic compression of solids using pulsed magnetic loading. *Rev Sci Instrum* 72:3587
  49. Asay J, Conf AIP (2000) Isentropic compression experiments on the Z accelerator. *AIP Conf Proc* 505:261
  50. Knudson M, Conf AIP (2012) Megaamps, megagauss and megabars: using the sandia Z machine to perform extreme material dynamics experiments. *AIP Conf Proc* 1426:35
  51. Lemke R, Knudson M, Davis J-P (2011) Magnetically driven hyper-velocity launch capability at the sandia Z accelerator. *Int J Impact Eng* 38:480
  52. Lemke R, Knudson M, Bliss D, Cochrane K, Davis J-P, Giunta A, Harjes H, Slutz S (2005) Magnetically accelerated, ultrahigh velocity flyer plates for shock wave experiments. *J Appl Phys* 98:073530
  53. Barker L, Hollenbach R (1972) Laser interferometer for measuring high velocities of any reflecting surface. *J Appl Phys* 43:4669
  54. Robinson A, Brunner T, Carroll S, Drake R, Garasi C, Gardiner T, Hail T, Hanshaw H, Hensinger D, Labreche D, Lemke R, Love E, Luchini C, Mosso S, Niederhaus J, Ober C, Petney S, Rider W, Scovazzi G, Strack O, Summers R, Trucano T, Weirs V, Wong M, Voth T (2008) (American Institute of Aeronautics and Astronautics, Inc., Reno, NV), ALEGRA: An arbitrary Lagrangian-Eulerian multimaterial, multiphysics code, in *proceedings of the 46th AIAA aerospace sciences meeting and exhibit*
  55. Brown J, Davis JP, Seagle C (2020) Multi-megabar dynamic strength measurements of Ta, Au, Pt, and Ir. *J Dynam Behav Mater* 7:196
  56. Asay J, Ao T, Vogler T, Davis J-P, Gray G III (2009) Yield strength of tantalum for shockless compression to 18 GPa. *J Appl Phys* 106:073515
  57. Vogler T, Ao T, Asay J (2009) High-pressure strength of aluminum under quasi-isentropic loading. *Int J Plast* 25:671
  58. Cowperthwaite M, Williams R (1971) Determination of constitutive relationships with multiple gauges in nondivergent waves. *J Appl Phys* 42:456
  59. von Mises R (1913) *Mechanik der festen Körper im pastisch-deformablen Zustand*. Nachrichten von der Gesellschaft der Wissenschaften zu Göttingen, Mathematisch-Physikalische Klasse 1:582
  60. Fowles G (1961) Shock wave compression of hardened and annealed 2024 aluminum. *J Appl Phys* 32:1475
  61. Asay J, Chhabildas L (1981) *Shock waves and high-strain-rate phenomena in metals*, edited by M. Meyers and L. Murr, Plenum, New York pp 417–431
  62. Specht P, Reinhart W, Alexander C (2022) Measurement of the hughoniot and shock-induced phase transition stress in wrought 17-4 H1025 stainless steel. *J Appl Phys* 131:125101
  63. Asay J, Lipkin J (1978) A self-consistent technique for estimating the dynamic yield strength of a shock-loaded material. *J Appl Phys* 49:4242
  64. Brown N, Specht P, Brown J (2022) Quasi-isentropic compression of an additively manufactured aluminum alloy to 14.8 GPa. *J Appl Phys* 132:225106
  65. Davis J-P, Knudson M, Shulenburg L, Crockett S (2016) Mechanical and optical response of [100] lithium fluoride to multi-megabar dynamic pressures. *J Appl Phys* 120:165901
  66. Davis J-P, Knudson M, Conf AIP (2009) Multi-megabar measurements of the principle quasi-isentropic for tantalum. *AIP Conf Proc* 1195:673
  67. Adams B, Bohnhoff W, Dalbey K, Ebeida M, Eddy J, Eldred M, Hooper R, Hough P, Hu K, Jakeman J, Khalil M, Maupin K, Mon-schke J, Ridgway E, Rushdi A, Seidl D, Stephens J, Swiler L, Tran A, Winokur J (Sandia National Laboratories, 2022) "Dakota, a multilevel parallel object-oriented framework for design optimization, parameter estimation, uncertainty quantification, and sensitivity analysis, version 6.16 user's manual", Tech. Rep. SAND2022-6171
  68. Carpenter J "Private communication",
  69. Steinberg D, Cochran S, Guinan M (1980) A constitutive model for metals applicable at high-strain rate. *J Appl Phys* 51:1498
  70. Steinberg D (Lawrence Livermore National Laboratory, 1996) "Equation of state and strength properties of selected materials", Tech. Rep. UCRL-MA-106439

71. Johnson J, Hixon R, Gray G III, Morris C (1992) Quasielastic release in shock-compressed solids. *J Appl Phys* 72:429
72. Cochrane KR, Lemke RW, Riford Z, Carpenter JH (2016) Magnetically launched flyer plate technique for probing electrical conductivity of compressed copper. *J Appl Phys* 119:105902
73. Crockett S, Rudin S ( Los Alamos National Laboratory, 2006) "Lithium fluoride equation of state (sesame 7271)I", Tech. Rep. LA-UR-06-8401
74. Ao T, Knudson M, Asay J, Davis J-P (2009) Strength of lithium fluoride under shockless compression to 114 GPa. *J Appl Phys* 106:103507
75. Holian K ( Los Alamos National Laboratory, 1984) " T-4 handbook of material properties data bases", Tech. Rep. LA-10160-MS
76. Lyon S, Johnson J ( Los Alamos National Laboratory, 1992) " SESAME: The Los Alamos National Laboratory equation of state database", Tech. Rep. LA-US-92-3407
77. Kraus R, Davis J-P, Seagle C, Frantanduono D, Swift D, Brown J, Eggert J (2016) Dynamic compression of copper to over 4560 GPa: a high-pressure standard. *Phys Rev B* 93:134105
78. Vinet P, Ferrante J, Smith J, Rose J (1986) A universal equation of state for solids. *J Phys C Solid State* 19:L467
79. Vinet P, Smith J, Ferrante J, Rose J (1987) Temperature effects on the universal equation of state of solids. *Phys Rev B* 35:1945
80. Vinet P, Rose J, Ferrante J, Smith J (1989) Universal features of the equation of state of solids. *J Phys -Condens Matter* 1:1941
81. Preston D, Tonks D, Wallace D (2003) Model of plastic deformation for extreme loading conditions. *J Appl Phys* 93:211
82. Brown J, Prime M, Barton N, Luscher D, Burakovsky L, Orlikowski D (2020) Experimental evaluation of shear modulus scaling of dynamic strength at extreme pressures. *J Appl Phys* 128:045901

**Publisher's Note** Springer Nature remains neutral with regard to jurisdictional claims in published maps and institutional affiliations.

Springer Nature or its licensor (e.g. a society or other partner) holds exclusive rights to this article under a publishing agreement with the author(s) or other rightsholder(s); author self-archiving of the accepted manuscript version of this article is solely governed by the terms of such publishing agreement and applicable law.